Microscopic description of octupole shape-phase transitions in light actinide and rare-earth nuclei

Nomura, Kosuke; Vretenar, Dario; Nikšić, Tamara; Lu, Bing-Nan

PHYSICAL REVIEW C **89**, 024312 (2014)

Microscopic description of octupole shape-phase transitions in light actinide and rare-earth nuclei

K. Nomura,[1] D. Vretenar,[2] T. Nikšić,[2] and Bing-Nan Lu[3]

[1]*Grand Accélérateur National d'Ions Lourds, CEA/DSM-CNRS/IN2P3, B.P. 55027, F-14076 Caen Cedex 5, France*

[2]*Physics Department, Faculty of Science, University of Zagreb, 10000 Zagreb, Croatia*

[3]*Institut für Kernphysik, Institute for Advanced Simulation, and Jülich Center for Hadron Physics, Forschungszentrum Jülich, D-52425 Jülich, Germany*

(Received 6 December 2013; revised manuscript received 4 February 2014; published 24 February 2014)

A systematic analysis of low-lying quadrupole and octupole collective states is presented based on the microscopic energy density functional framework. By mapping the deformation constrained self-consistent axially symmetric mean-field energy surfaces onto the equivalent Hamiltonian of the sdf interacting boson model (IBM), that is, onto the energy expectation value in the boson condensate state, the Hamiltonian parameters are determined. The study is based on the global relativistic energy density functional DD-PC1. The resulting IBM Hamiltonian is used to calculate excitation spectra and transition rates for the positive- and negative-parity collective states in four isotopic chains characteristic for two regions of octupole deformation and collectivity: Th, Ra, Sm, and Ba. Consistent with the empirical trend, the microscopic calculation based on the systematics of β_2-β_3 energy maps, the resulting low-lying negative-parity bands and transition rates show evidence of a shape transition between stable octupole deformation and octupole vibrations characteristic for β_3-soft potentials.

DOI: 10.1103/PhysRevC.89.024312 PACS number(s): 21.10.Re, 21.60.Ev, 21.60.Fw, 21.60.Jz

I. INTRODUCTION

The study of equilibrium shapes and shape transitions presents a recurrent theme in nuclear structure physics [1–3]. Even though most deformed medium-heavy and heavy nuclei exhibit quadrupole, reflection-symmetric equilibrium shapes, there are regions in the mass table where octupole deformations (reflection-asymmetric, pear-like shapes) occur (see [4] for a review). In particular, nuclei with neutron (proton) number N (Z) $\approx$ 34, 56, 88, and 134 [4]. Reflection-asymmetric shapes are characterized by the presence of negative-parity bands, and by pronounced electric dipole and octupole transitions. In the case of static octupole deformation, for instance, the lowest positive-parity even-spin states and the negative-parity odd-spin states form an alternating-parity band, with states connected by the enhanced $E1$ transitions.

In a simple microscopic picture octupole deformation is expected to develop through a coupling of orbitals in the vicinity of the Fermi surface with quantum numbers (l, j) and an intruder unique-parity orbital with ($l+3$, $j+3$) [4]. For instance, in the case of heavy ($Z \approx 88$ and $N \approx 134$) nuclei in the region of light actinides, the coupling of the neutron orbitals $g_{9/2}$ and $j_{15/2}$, and that of the proton single-particle states $f_{7/2}$ and $i_{13/2}$, can lead to octupole mean-field deformations. Structure phenomena related to reflection-asymmetric nuclear shapes have been extensively investigated in numerous experimental studies [4,5]. In particular, very recently clear evidence for pronounced octupole deformation in the region $Z \approx 88$ and $N \approx 134$, e.g., in ^{220}Rn and ^{224}Ra, has been reported in Coulomb excitation experiments with radioactive ion beams [6]. Also in the rare-earth region ($Z \approx 56$ and $N \approx 88$), a recent experiment [7] has revealed low-energy negative-parity bands in ^{152}Sm. The renewed interest in studies of reflection asymmetric nuclear shapes using accelerated radioactive beams [6] point to the significance of a timely systematic theoretical analysis of quadrupole-octupole collective states of nuclei in several mass regions of the nuclear chart where octupole shapes are expected to occur.

A variety of theoretical methods have been applied to studies of reflection asymmetric shapes and the evolution of the corresponding negative-parity collective states. These include self-consistent mean-field models [8–17], algebraic (or interacting boson) models [18–22], phenomenological collective models [23–30], and cluster models [31–33]. In particular, a great number of self-consistent mean-field calculations of nuclei with static or dynamic octupole deformations have been reported, e.g., based on the Nilsson-Strutinsky method [9], Skyrme [11,12] and Gogny [13–17] effective interactions, and relativistic mean-field (RMF) models [34–36].

Nuclear energy density functionals (EDFs) enable a complete and accurate description of ground-state properties and collective excitations over the whole nuclide chart [37]. Both nonrelativistic [38–40] and relativistic [41,42] EDFs have been successfully applied to the description of the evolution of single-nucleon shell structures and the related shape-transition and shape-coexistence phenomena. To compute excitation spectra and transition rates, however, the EDF framework has to be extended to take into account the restoration of symmetries broken in the mean-field approximation, and fluctuations in the collective coordinates. In this study we employ a recently developed method [43] for determining the Hamiltonian of the interacting boson model (IBM) [44], starting with a microscopic, EDF-based self-consistent mean-field calculation of deformation energy surfaces. By mapping the deformation constrained self-consistent energy surfaces onto the equivalent Hamiltonian of the IBM, that is, onto the energy expectation value in the boson condensate state, the Hamiltonian parameters are determined. The resulting IBM Hamiltonian is used to calculate excitation spectra and transition rates. This technique has been extended and applied to study moments of inertia of deformed rotational nuclei [45], to analyze the γ-softness in medium-heavy and heavy nuclei

[46], and to describe coexistence and mixing of different intrinsic shapes [47]. More recently the method of [43] has been applied to a study of the octupole shape-phase transition in the Th isotopic chain [48].

This work extends the study of Ref. [48] and presents a microscopic analysis of octupole shape transitions in four isotopic chains characteristic for two regions of octupole deformation and collectivity: Th, Ra, Sm, and Ba. The study is based on the microscopic framework of nuclear energy density functionals (EDFs), and the Hamiltonian of the sdf IBM [19,49] is determined from axial quadrupole-octupole deformation energy surfaces calculated employing the relativistic Hartree-Bogoliubov model based on the universal energy density functional DD-PC1 [50]. The mapped sdf IBM Hamiltonian is used to calculate low-energy spectra and transition rates for both positive- and negative-parity states of the four sequences of isotopes. The semimicroscopic relativistic functional DD-PC1 was adjusted to the experimental masses of a set of 64 deformed nuclei in the mass regions $A \approx 150$–180 and $A \approx 230$–250, and further tested in a number of mean-field and beyond-mean-field calculations in different mass regions.

The article is organized as follows. In Sec. II we describe the theoretical framework. The systematics of self-consistent mean-field results and the quality of the mapping onto the IBM are described in Sec. III. Spectroscopic properties calculated with the mapped sdf IBM Hamiltonian are discussed in Sec. IV, including the systematics of low-lying positive- and negative-parity states, $E1$, $E2$, and $E3$ transitions, and detailed level schemes of selected nuclei. Section V contains the summary and concluding remarks.

II. DESCRIPTION OF THE MODEL

The analysis starts by performing constrained self-consistent relativistic mean-field calculations for axially symmetric shapes in the (β_2,β_3) plane, with constraints on the mass quadrupole Q_{20} and octupole Q_{30} moments. The dimensionless shape variables β_λ ($\lambda = 2,3$) are defined in terms of the multipole moments $Q_{\lambda 0}$:

$$\beta_\lambda = \frac{4\pi}{3AR^\lambda} Q_{\lambda 0} \tag{1}$$

with $R = 1.2A^{1/3}$ fm. The relativistic Hartree-Bogoliubov (RHB) model [41] is used to calculate constrained energy surfaces, the functional in the particle-hole channel is DD-PC1, and pairing correlations are taken into account by employing an interaction that is separable in momentum space, and is completely determined by two parameters adjusted to reproduce the empirical bell-shaped pairing gap in symmetric nuclear matter [42,51]. For technical details of the calculation of self-consistent RHB energy surfaces, the reader is referred to Refs. [35,36]. In this work the energy surface in RHB calculations refers to the total energy of the nuclear system as a function of deformation parameters.

A quantitative study of low-lying quadrupole and octupole collective states must go beyond a simple mean-field calculation of energy surfaces and take into account collective correlations related to restoration of symmetries broken by the mean field and quantum fluctuations in deformation variables. To this end we employ the interacting boson model (IBM) [44] to analyze spectroscopic properties associated to both quadrupole and octupole collective degrees of freedom. The building blocks of the most standard version of the IBM that includes quadrupole degrees of freedom are the monopole s and quadrupole d bosons, that correspond to $J^\pi = 0^+$ and 2^+ collective pairs of valence nucleons, respectively [52]. To describe reflection-asymmetric deformations and the corresponding negative-parity states, in addition to these positive-parity bosons the model space must include the octupole ($J^\pi = 3^-$) f boson [19,49].

A general IBM Hamiltonian of the sdf system contains interaction terms acting in the sd and f boson spaces, and the coupling between the two spaces [49]:

$$\hat{H} = \hat{H}_{sd} + \hat{H}_f + \hat{H}_{sdf}. \tag{2}$$

In the present analysis we employ the following terms:

$$\hat{H}_{sd} = \epsilon_d \hat{n}_d + \kappa_2 \hat{Q}_{sd} \cdot \hat{Q}_{sd} + \alpha \hat{L}_d \cdot \hat{L}_d \tag{3}$$

with $\hat{n}_d = d^\dagger \cdot \tilde{d}$, $\hat{Q}_{sd} = s^\dagger \tilde{d} + d^\dagger s + \chi_d [d^\dagger \times \tilde{d}]^{(2)}$, and $\hat{L}_d = \sqrt{10}[d^\dagger \times \tilde{d}]^{(1)}$ denoting the d-boson number operator, the quadrupole operator, and the angular momentum operator for the sd boson space, respectively:

$$\hat{H}_f = \epsilon_f \hat{n}_f + \kappa_2' \hat{Q}_f \cdot \hat{Q}_f \tag{4}$$

$\hat{n}_f = f^\dagger \cdot \tilde{f}$ is the f-boson number operator, and $\hat{Q}_f = \chi_f [f^\dagger \times \tilde{f}]^{(2)}$ denotes the quadrupole f-boson interaction. Finally,

$$\hat{H}_{sdf} = \kappa_2'' \hat{Q}_{sd} \cdot \hat{Q}_f + \kappa_3 : \hat{V}_3^\dagger \cdot \hat{V}_3 :, \tag{5}$$

where the last term is the octupole-octupole interaction written in the normal-ordered form with $\hat{V}_3^\dagger = s^\dagger \tilde{f} + \chi_3 [d^\dagger \times \tilde{f}]^{(3)}$. In the present calculation $\kappa_2' = \kappa_2''/2 = \kappa_2$. The Hamiltonians of Eqs. (3) and (4) have been used in a number of phenomenological IBM studies of low-energy quadrupole and octupole collective states. The coupling Hamiltonian Eq. (5) is similar to the one used in Ref. [53], and can be derived from a microscopic octupole-octupole interaction between neutron and the proton bosons by mapping the totally symmetric state of the IBM-2 system to the corresponding state in the IBM-1 [53]. In this work, however, the dipole-dipole interaction term $\hat{L}_d \cdot \hat{L}_f$ (with $\hat{L}_f = \sqrt{28}[f^\dagger \times \tilde{f}]^{(1)}$) is not included, as it has been shown [22] to be of little relevance for low-lying collective states. In contrast to previous sdf IBM phenomenological studies, in which the maximum number of f bosons $N_f^{\max}$ has been kept constant to reduce the model space and thus computing time ($N_f^{\max} = 1$ in most cases), in the present analysis both positive- and negative-parity bosons are treated in the same way, that is, there is no truncation specific for the f-boson number. The total number of bosons $s + d + f$ is determined by the number of valence proton and neutron pairs.

We also note that some empirical IBM studies suggested the importance of including the p ($J^\pi = 1^-$) boson to improve the agreement with experimental results (for instance, [20,54,55]), particularly for the $E1$ properties. From the algebraic point of view it was shown [19] that the p boson is necessary to obtain the SU(3) dynamical symmetry of the U(16) group. On the

other hand, the microscopic origin of the p boson has been related either to the spurious center-of-mass motion [19], or to the giant dipole resonance [56]. Here we do not include the p boson in the model space, as in fact neither of these degrees of freedom are particularly relevant for an analysis based on microscopic mean-field calculations.

For each nucleus the parameters of the Hamiltonian: ϵ_d, ϵ_f, κ_2, κ_3, χ_d, χ_f, and χ_3, are determined from the microscopic RHB energy surfaces employing the procedure of Ref. [43,57]: the microscopic constrained self-consistent mean-field energy surface is mapped onto the equivalent IBM energy surface, that is, on the expectation value of the IBM Hamiltonian $\langle\phi|\hat{H}|\phi\rangle$ in the boson condensate state $|\phi\rangle$ [58]:

$$|\phi\rangle = \frac{1}{\sqrt{N_B!}}(\lambda^\dagger)^{N_B}|-\rangle \quad \text{with} \quad \lambda^\dagger = s^\dagger + \bar{\beta}_2 d_0^\dagger + \bar{\beta}_3 f_0^\dagger \,. \tag{6}$$

N_B and $|-\rangle$ denote the total number of bosons, that is, half the number of valence nucleons [52], and the boson vacuum (inert core), respectively. $\bar{\beta}_2$ and $\bar{\beta}_3$ represent the axial quadrupole and octupole shape variables in the boson system, respectively, equivalent to the deformation parameters of Eq. (1) that are used to characterize the RHB energy surfaces. However, since the model spaces of the RHB and the IBM are different, one finds that generally $\bar{\beta}_\lambda$ is also different from β_λ [58]. For $\lambda = 2$, the proportionality $\bar{\beta}_2 \equiv C_2\beta_2$, with C_2 being a coefficient, appears to be a good approximation [43,58]. Here we further assume that, independently of the $\lambda = 2$ deformation, a similar relation also holds for $\lambda = 3$, that is, $\bar{\beta}_3 \equiv C_3\beta_3$. The coefficients $C_{\lambda=2,3}$ are determined basically by adjusting the location of the minimum on the (β_2,β_3) energy surface. In the present study, the doubly-magic nuclei ^{208}Pb and ^{132}Sn are taken as inert cores for the considered regions of Th-Ra and Sm-Ba nuclei, respectively. Therefore, N_B takes values from 6 to 12, from 5 to 10, from 7 to 12, and from 4 to 9 for $^{220-232}$Th, $^{218-228}$Ra, $^{146-156}$Sm, and $^{140-150}$Ba, respectively. The analytic expression for the expectation value of the IBM Hamiltonian reads

$$\begin{aligned} E(\bar{\beta}_2,\bar{\beta}_3) = {} & \frac{N_B}{1+\bar{\beta}_2^2+\bar{\beta}_3^2}\left(\epsilon'_s + \epsilon'_d\bar{\beta}_2^2 + \epsilon'_f\bar{\beta}_3^2\right) \\ & + \frac{N_B(N_B-1)}{\left(1+\bar{\beta}_2^2+\bar{\beta}_3^2\right)^2} \\ & \times\left[\kappa_2\left(2\bar{\beta}_2 - \sqrt{\frac{2}{7}}\chi_d\bar{\beta}_2^2 - \frac{2}{\sqrt{21}}\chi_f\bar{\beta}_3^2\right)^2\right. \\ & \left. + 4\kappa_3\left(\bar{\beta}_3 - \frac{2}{\sqrt{15}}\chi_3\bar{\beta}_2\bar{\beta}_3\right)^2\right], \end{aligned} \tag{7}$$

with

$$\epsilon'_s = 5\kappa_2, \quad \epsilon'_d = \epsilon_d + 6\alpha + \left(1+\chi_d^2\right)\kappa_2$$
$$\text{and} \quad \epsilon'_f = \epsilon_f + \frac{5}{7}\kappa_2\chi_f^2. \tag{8}$$

By equating the energy expectation value as a function of the quadrupole and octupole deformation parameters to the microscopic energy surface in the neighborhood of the energy minimum (typically up to 2 MeV from the minimum), the IBM Hamiltonian parameters can be determined without invoking any phenomenological adjustment to experiment.

The coupling constant of the $\hat{L}_d \cdot \hat{L}_d$ term, α, is adjusted separately in such a way that the cranking moment of inertia calculated in the boson intrinsic state on the $\beta_3 = 0$ axis becomes identical to the corresponding one obtained from the mean-field model [45].

The resulting sdf IBM Hamiltonian is diagonalized employing the code OCTUPOLE [59]. This generates the excitation spectra and, subsequently, electromagnetic transition rates, that is, the reduced transition probabilities $B(E\lambda; J \to J')$:

$$B(E\lambda; J \to J') = \frac{1}{2J+1}|\langle J'||\hat{T}^{(E\lambda)}||J\rangle|^2, \tag{9}$$

with $|J\rangle$ ($|J'\rangle$) being the wave function for the initial (final) state with spin J (J'). The $E1$, $E2$, and $E3$ operators, denoted here $\hat{T}^{(E1)}$, $\hat{T}^{(E2)}$, and $\hat{T}^{(E3)}$, respectively, are defined as follows:

$$\hat{T}^{(E1)} = e_1(d^\dagger \times \tilde{f} + f^\dagger \times \tilde{d})^{(1)}, \tag{10}$$

$$\hat{T}^{(E2)} = e_2\hat{Q}, \tag{11}$$

where $\hat{Q} = \hat{Q}_{sd} + \hat{Q}_f$, and the parameters χ_d and χ_f are consistently the same as the ones used in the Hamiltonian and, finally,

$$\hat{T}^{(E3)} = e_3(\hat{V}_3^\dagger + \hat{V}_3). \tag{12}$$

The operator $\hat{V}_3^\dagger$ is defined in Eq. (5), and again the same value for χ_3 is consistently used in the Hamiltonian and $E3$ operator. e_1, e_2, and e_3 denote the corresponding effective charges. Their values are $e_1 = 0.01\ e\text{b}^{1/2}$ (taken from [60]) for all nuclei considered, $e_2 = 0.19\ e$b (from [20]), and $0.13\ e$b (from [18]) for Th-Ra and Sm-Ba isotopes, respectively. The values $e_3 = 0.15\ e\text{b}^{3/2}$ for Th-Ra and $e_3 = 0.09\ e\text{b}^{3/2}$ for Sm-Ba isotopes are adjusted to reproduce the overall trend of experimental results.

From the calculated $B(E\lambda; J \to J')$ values, one obtains the transition intrinsic moments $Q_\lambda(J \to J')$:

$$Q_\lambda(J \to J') = \sqrt{\frac{16\pi}{2\lambda+1}\frac{B(E\lambda; J \to J')}{(J\lambda 00|J'0)^2}}\,, \tag{13}$$

where $(J\lambda 00|J'0)$ denotes the Clebsch-Gordan coefficient.

III. MAPPING THE SELF-CONSISTENT MEAN-FIELD RESULTS ONTO THE IBM SPACE

A. Systematics of deformation energy surfaces

Figures 1–4 display the axially symmetric deformation energy surfaces in (β_2,β_3) plane, calculated with the constrained RHB using the microscopic functional DD-PC1, for the isotopes $^{222-232}$Th, $^{218-228}$Ra, $^{146-156}$Sm, and $^{140-150}$Ba, respectively. Each energy surface is plotted up to 10 MeV excitation above its absolute minimum, and is symmetric with respect to the $\beta_3 = 0$ axis. We note that, in Figs. 1 and 5, the energy surface of ^{220}Th is not shown, as it is very similar to the one calculated for the adjacent nucleus ^{222}Th.

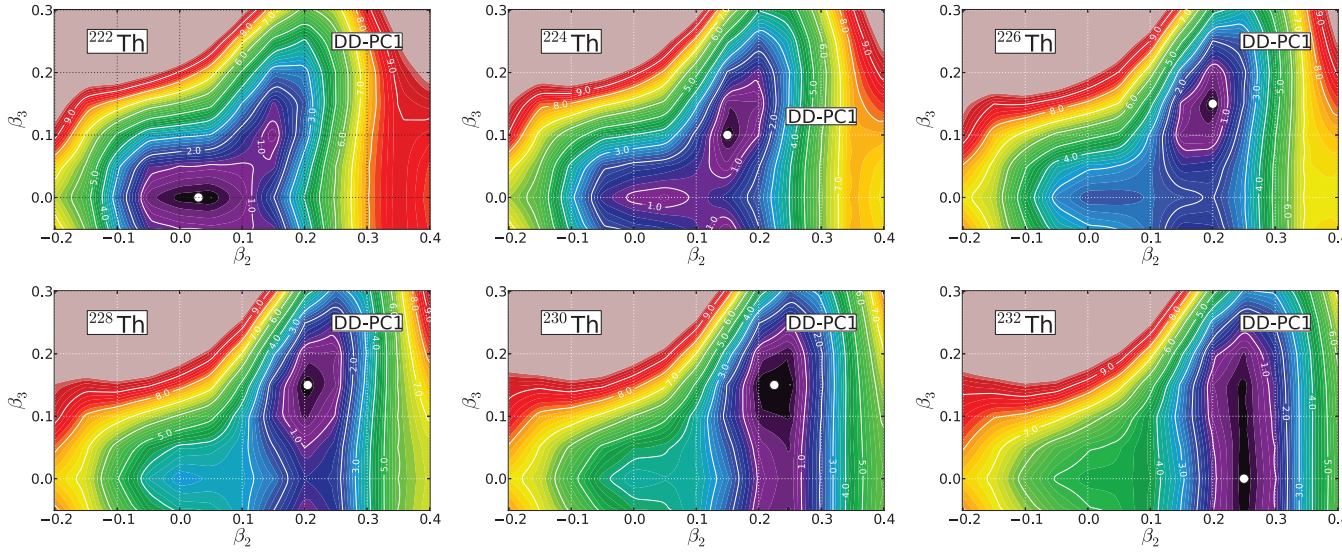

FIG. 1. (Color online) Axially symmetric energy surfaces of the isotopes $^{222–232}$Th in the (β_2,β_3) plane, calculated using the self-consistent RHB model with the microscopic functional DD-PC1. The contours join points on the surface with the same energy (in MeV), and the color scale varies in steps of 0.2 MeV. The energy difference between neighboring contours is 1 MeV. Note that energy surfaces are symmetric with respect to the $\beta_3 = 0$ axis. Open circles denote the absolute energy minima.

In Fig. 1 we note that already at the mean-field level the RHB calculation predicts a very interesting structural evolution in Th isotopic chain. A soft energy surface is calculated for ^{222}Th, with the minimum in the region $(\beta_2,\beta_3) \approx (0,0)$, and this will typically lead to low-lying quadrupole vibrational spectra. Quadrupole deformation becomes significant in ^{224}Th, and one also notices the emergence of octupole deformation. The energy minimum is found in the $\beta_3 \neq 0$ region, located at $(\beta_2,\beta_3) \approx (0.15,0.1)$. From ^{224}Th to ^{226,228}Th the occurrence of a rather strongly marked octupole minimum is predicted. The deepest octupole minimum is calculated in ^{226}Th whereas, starting from ^{228}Th, the minimum becomes softer in β_3 direction. Octupole-soft surfaces are obtained for ^{230,232}Th, the latter being completely flat in β_3. In previous calculations of Th isotopes with the Nilsson-Strutinsky method that used a deformed Woods-Saxon potential [9,10], a quadrupole vibrational shape was obtained for ^{220}Th, and a stable octupole deformation was predicted to occur in $^{222–226}$Th. In those studies, the most pronounced octupole minimum was calculated in ^{224}Th, a soft octupole shape was obtained for ^{228}Th and, finally, a shape without equilibrium octupole deformation for ^{230}Th.

The DD-PC1 energy surfaces of Ra isotopes, shown in Fig. 2, display a more gradual evolution of octupole deformation as a function of mass number, and the most pronounced octupole minimum is predicted in ^{224}Ra in the region $(\beta_2,\beta_3) \approx (0.15–0.2,0.10–0.15)$: absolute minimum is found at $(\beta_2,\beta_3) \approx (0.2,0.15)$, while the second minimum,

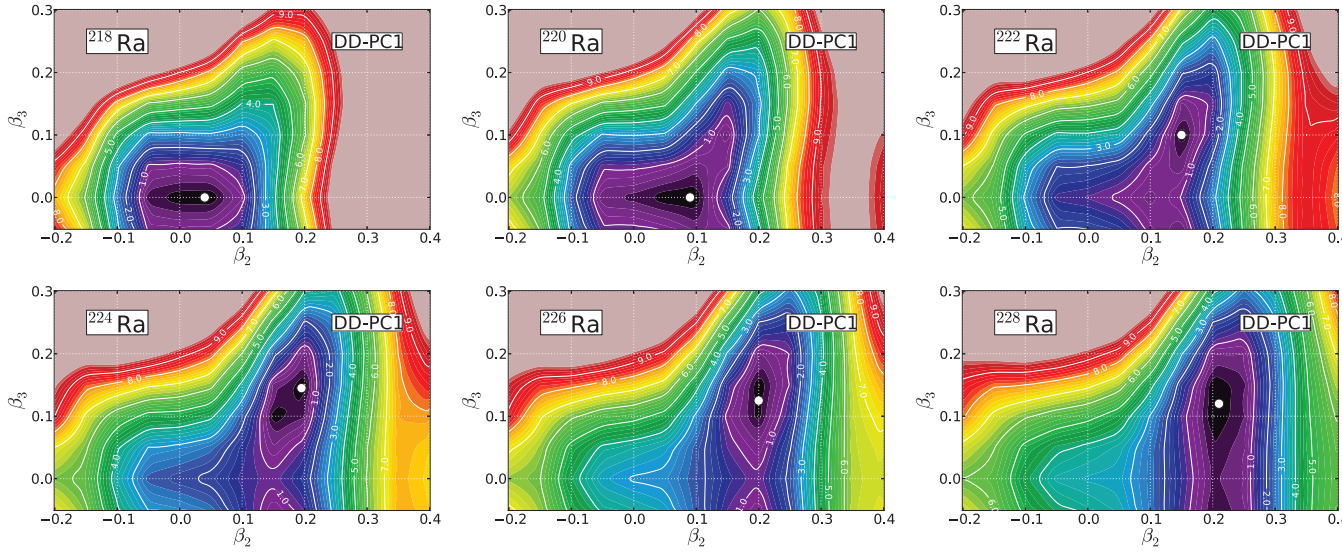

FIG. 2. (Color online) Same as the caption to Fig. 1, but for $^{218–228}$Ra.

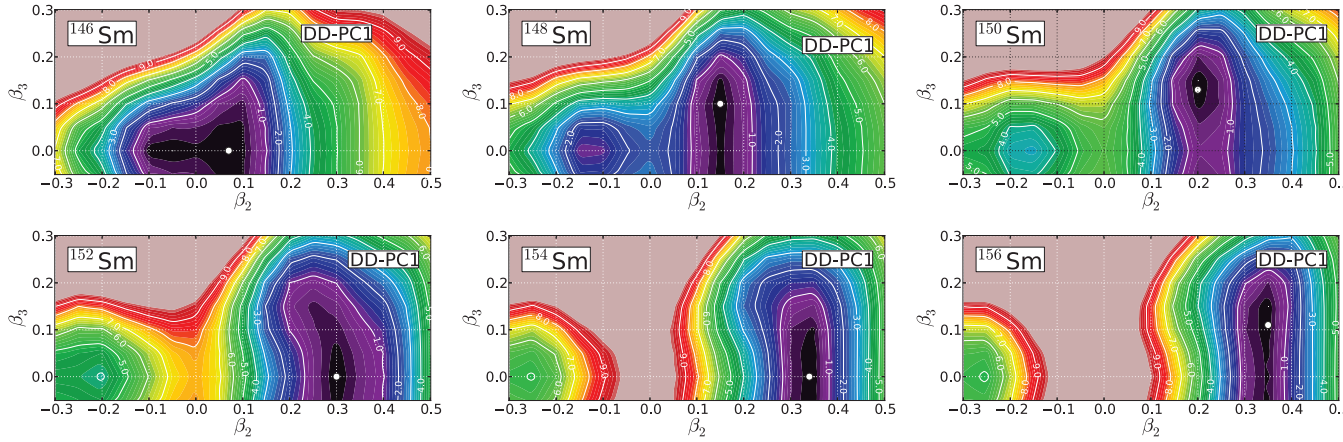

FIG. 3. (Color online) Same as the caption to Fig. 1, but for $^{146-156}$Sm.

which is very close in energy, locates at $(\beta_2,\beta_3) \approx (0.15,0.10)$. These values, particularly the latter one, are rather consistent with the equilibrium deformation $\beta_2 = 0.154$ and $\beta_3 = 0.097$, extracted from the experimentally determined intrinsic moments Q_2 and Q_3, respectively, in Ref. [6]. The minimum becomes softer in β_3 for ^{226}Ra, and a completely β_3-soft potential is predicted in ^{228}Ra, characteristic for the onset of octupole vibrations. We note that previous mean-field calculations based on the Nilsson-Strutinsky method [9], and the constrained Hartree-Fock-Bogoliubov method [14] with the Gogny D1S [61] and the Barcelona-Catania-Paris (BCP) [62] effective interactions, predicted the occurrence of the most prominent octupole equilibrium deformation in ^{222}Ra.

In the other mass region considered in the present study, the RHB results for Sm isotopes, shown in Fig. 3, exhibit a simultaneous evolution of both quadrupole and octupole deformations with increasing neutron number. A stable octupole minimum is predicted to occur in ^{150}Sm, and the deformation energy surface becomes soft in β_3 for the heavier isotopes. A similar systematic trend was also obtained in a recent analysis that used the relativistic mean-field plus BCS model [34], based on the PK1 parameter set [63]. In Fig. 4 we plot the DD-PC1 deformation energy surfaces for Ba isotopes. Pronounced octupole minima are predicted starting from ^{144,146}Ba but, in contrast to the evolution of β_3-softness in Sm nuclei, the deformation of the energy surface does not become much softer in β_3 for heavier isotopes. Shallow octupole equilibrium minima are obtained in ^{146}Ba–^{150}Ba. The evolution of quadrupole and octupole deformations in the Ba isotopes predicted by the functional DD-PC1, and in particular the octupole minimum in ^{144,146}Ba, is consistent with previous mean-field calculations based on the Nilsson-Strutinsky method [9] and the Gogny D1S effective interaction [14]. Both studies, however, predicted the disappearance of the octupole minimum in ^{150}Ba, whereas a shallow minimum with a nonzero β_3 value is predicted in the present calculation.

Figures 5–8 display the corresponding IBM energy surfaces of Th, Ra, Sm, and Ba, mapped from the self-consistent mean-field results shown in Figs. 1–4. As an illustrative example we discuss in more detail the Th isotopes. Figure 5 shows that the mapping reproduces the evolution of octupole minima as a function of neutron number: the quadrupole minimum for ^{222}Th, the onset of octupole minimum in ^{224}Th, the pronounced octupole deformation in ^{226,228}Th, and the soft-octupole potential for ^{230,232}Th, originally displayed by the microscopic energy surfaces in Fig. 1. If one considers in detail each individual nucleus, particularly the heavier Th isotopes with $A \geqslant 226$, it can be noticed that the topology of the mapped

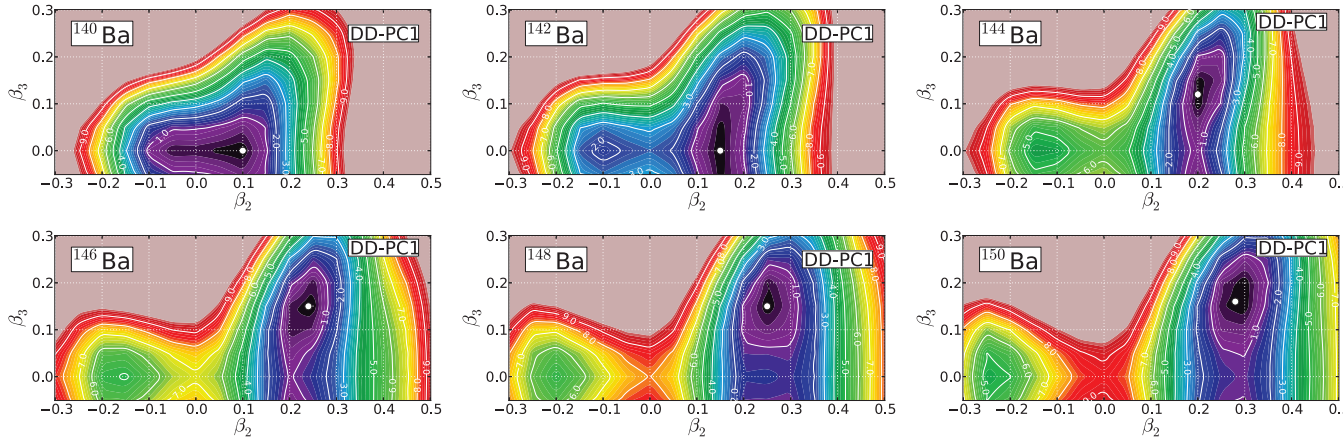

FIG. 4. (Color online) Same as the caption to Fig. 1, but for $^{140-150}$Ba.

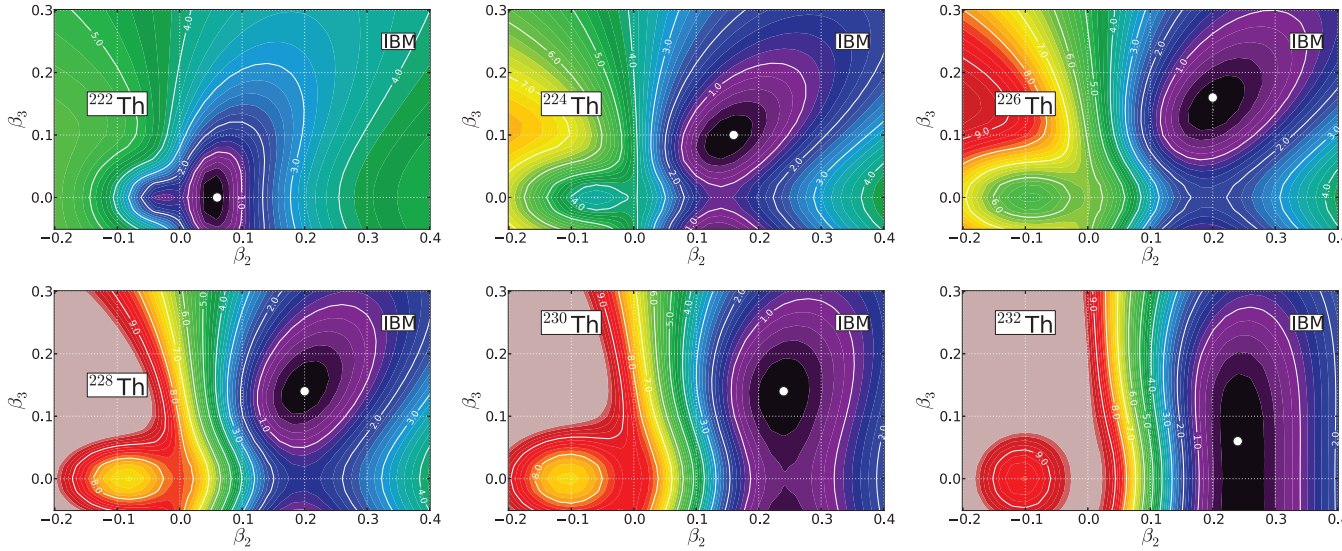

FIG. 5. (Color online) Same as the caption to Fig. 1, but for the mapped IBM energy surfaces of $^{222-232}$Th.

IBM energy surface reproduces the original microscopic surface in the region close to the minimum, whereas more pronounced differences between the microscopic and IBM energy surface are observed for $\beta_2 \leqslant 0.0$. The reason is that the IBM Hamiltonian is constructed in such a way that it reproduces only the neighborhood of the minimum of the microscopic energy surface, which is most relevant for the low-lying collective states considered in this work. The IBM energy surface of Eq. (7) cannot reproduce all the details of a more complex topology of the microscopic energy surface. One also notices that generally in regions very far from the minimum the mapped energy surfaces are more smooth in comparison to the microscopic ones, which is again due to the restricted boson model space of the IBM compared to the fermion space of the RHB framework. This is a general feature of the IBM approach and cannot be modified by simply readjusting the model parameters. In particular the deviations are more apparent for isotopes like ^{222,224}Th, that are characterized by a smaller boson number. For the other isotopic chains shown from Figs. 6 to 8, one should find more or less the same extent of similarity as for the Th chain between the DD-PC1 and the IBM energy surfaces. Nevertheless, for the Ra (Ba) nuclei, the IBM energy surfaces are shallower than for the Th (Sm) nuclei because the number of bosons is more limited.

Figure 9 displays the mass dependence of the average value of the octupole deformation $\langle\beta_3\rangle$ and the variance $\Delta\beta_3 = \sqrt{\langle\beta_3^2\rangle - \langle\beta_3\rangle^2}$, for $^{220-232}$Th, $^{218-228}$Ra, $^{146-156}$Sm, and $^{140-150}$Ba, obtained from the mapped IBM energy surfaces. The average octupole deformation and the variance are calculated over a region on the (β_2,β_3) plane that extends from the absolute mean-field minimum up to approximately 2 MeV excitation energy above the minimum. A prominent feature in Fig. 9(a) is the sudden increase of $\langle\beta_3\rangle$ from ^{222}Th

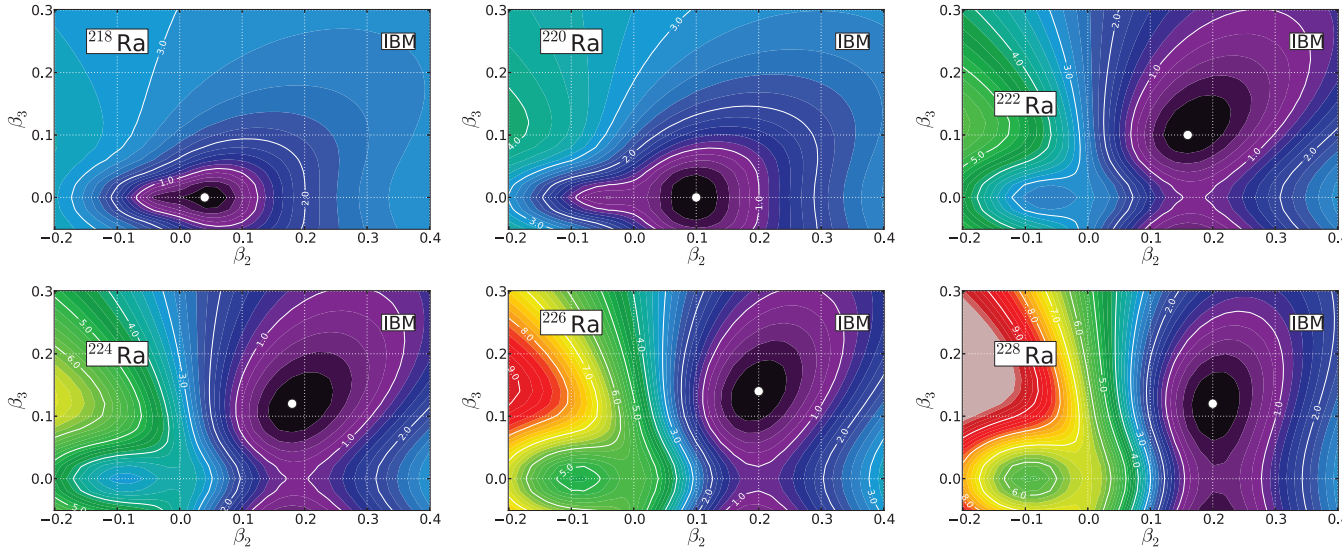

FIG. 6. (Color online) Same as the caption to Fig. 1, but for the mapped IBM energy surfaces of $^{218-228}$Ra.

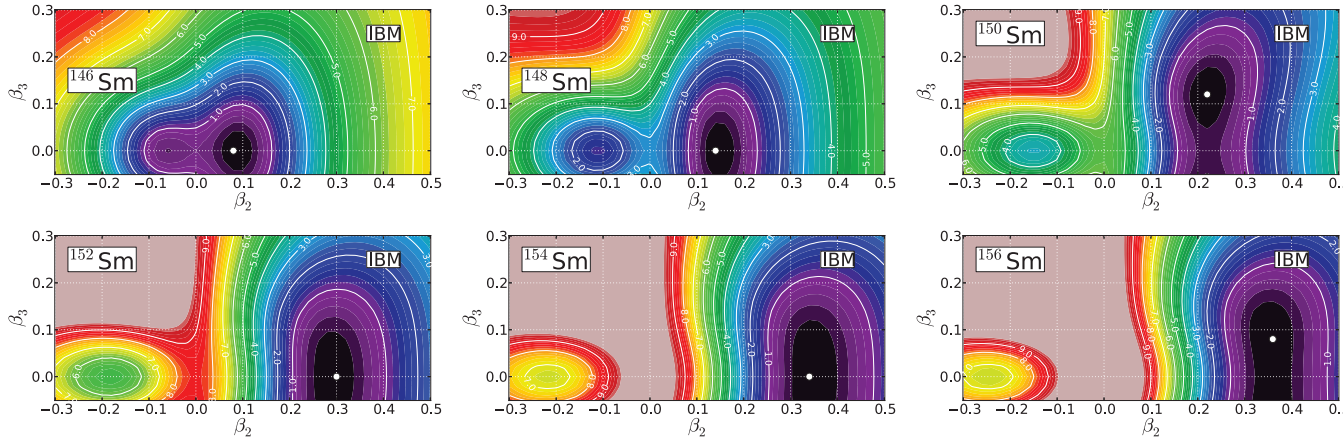

FIG. 7. (Color online) Same as the caption to Fig. 1, but for the mapped IBM energy surfaces of $^{146-156}$Sm.

to ^{224}Th, from ^{220}Ra to ^{222}Ra, from ^{148}Sm to ^{150}Sm, and from ^{142}Ba to ^{144}Ba. For these nuclei the energy minimum is suddenly displaced from the $\beta_3 \approx 0$ axis to the $\beta_3 \neq 0$ region. For each isotopic chain the value of $\langle\beta_3\rangle$ stabilizes at $\beta_3 \approx 0.15$ in heavier nuclei. The mass dependence of the variance $\Delta\beta_3$ in Fig. 9(b) reflects the fluctuation in the octupole deformation between the nonoctupole deformed shape and octupole deformation.

B. Parameters of the quadrupole-octupole IBM Hamiltonian

In Fig. 10 we plot the adopted parameters for the sdf IBM Hamiltonian Eq. (2): ϵ_d (a), ϵ_f (b), χ_d (b), χ_f (c), χ_f (d), and χ_3 (e), and the coefficient of the shape variables C_2 (f) and C_3 (g), determined by mapping the microscopic RHB energy surfaces onto the corresponding expectation values of the IBM Hamiltonian in the boson condensate state Eq. (6). One notices a certain trend in a variation of each parameter as a function of boson number, that correlates with the variation of the intrinsic shape (Figs. 1–8). The decrease of the d [Fig. 10(a)] and f [Fig. 10(b)] single-boson energies with N_B reflects the evolution of quadrupole and octupole collectivity, respectively. An interesting feature is that, while for Sm and Ba isotopes generally $\epsilon_d \leqslant \epsilon_f$ (consistent with the study of Ref. [60] for Sm isotopes), the values ϵ_d and ϵ_f are similar for the Th and Ra isotopic chains. This indicates that for the latter mass region octupole and quadrupole collectivity are comparable in magnitude.

Similarly to ϵ_d and ϵ_f, the values of the parameters χ_d [Fig. 10(c)] and χ_f [Fig. 10(d)] decrease with N_B and appear to saturate around $\chi_d = -1$ and $\chi_f = -2.5$. The former value is close to the SU(3) limit for the sd sector, $\chi_d = -\sqrt{7}/2$ [44]. For each chain the parameter χ_3 reaches a maximum in magnitude for a particular isotope, that is, for ^{226}Th ($N_B = 9$), ^{224}Ra ($N_B = 8$), ^{150}Sm ($N_B = 9$), and ^{144,146}Ba [$N_B = 6,7$ (Fig. 10(e)]. As expected from the analyses in Sec. III A, octupole deformation is most pronounced in these nuclei. By further increasing the number of bosons the magnitude of χ_3 generally decreases, reflecting the evolution of octupole softness (cf. Figs. 1–4). The scale parameters C_2 [Fig. 10(f)] and C_3 [Fig. 10(g)] evolve monotonically with N_B according to the change of the location of the energy minimum on the RHB energy surfaces.

The values of the remaining parameters κ_2, κ_3 and α are taken to be almost constant with respect to neutron number: $\kappa_2 \approx -0.06$ MeV for the Th-Ra isotopes, $\kappa_2 \approx -0.088 \sim -0.08$ MeV for Sm, and $\kappa_2 \approx -0.11 \sim -0.09$ for Ba; $\kappa_3 \approx 0.06$ MeV for Th-Ra, $\kappa_3 \approx 0.02$ MeV for Sm, and $\kappa_3 \approx 0.04$ MeV for the Ba isotopes; $\alpha \approx -0.02$ MeV for

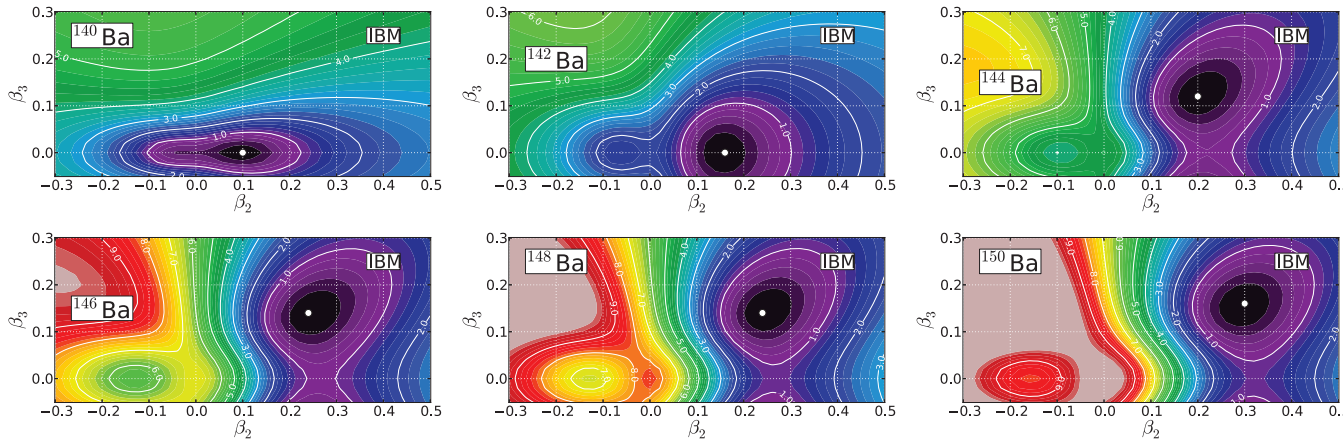

FIG. 8. (Color online) Same as the caption to Fig. 1, but for the mapped IBM energy surfaces of $^{140-150}$Ba.

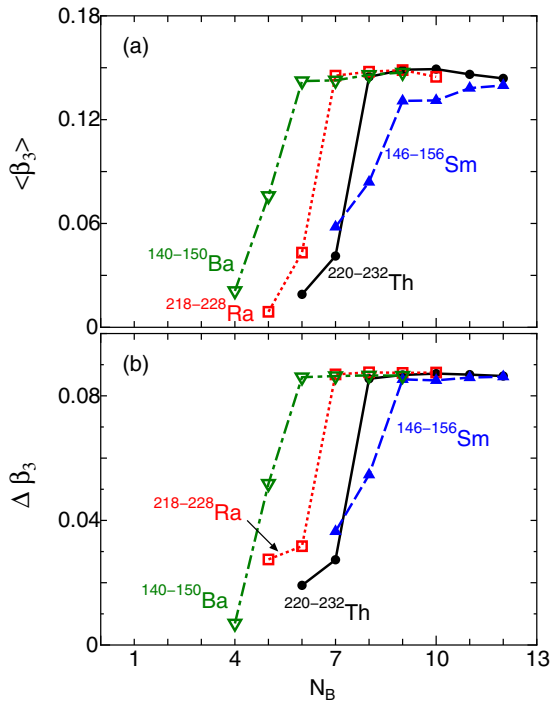

FIG. 9. (Color online) Mean value of the octupole deformation parameter $\langle\beta_3\rangle$ for $^{220-232}$Th, $^{218-228}$Ra, $^{146-156}$Sm, and $^{140-150}$Ba, computed with the IBM intrinsic state (a), and the corresponding variance $\Delta\beta_3 = \sqrt{\langle\beta_3^2\rangle - \langle\beta_3\rangle^2}$ (b), as functions of the boson number N_B.

Th-Ra, $^{152-156}$Sm and $^{146-150}$Ba, $\alpha \approx -0.01$ MeV for $^{146-150}$Sm and $^{140-144}$Ba.

IV. SPECTROSCOPIC PROPERTIES

A signature of static reflection-asymmetric shapes is a negative-parity $K^\pi = 0^-$ band with $J^\pi = 1^-,3^-,5^-,\ldots$, located close in energy to the positive-parity ground-state band $J^\pi = 0^+,2^+,4^+,\ldots$. One could say that the two sequences form a single alternating-parity band, with states connected by strong $E1$ transitions [4]. In most nuclei, however, the two bands are displaced from each other and an approximate alternating-parity band is experimentally observed only for states with higher spin, typically $J > 5$. In the case of dynamical octupole deformation the negative-parity band lies at considerably higher energy and the two sequences with $K^\pi = 0^+$ and $K^\pi = 0^-$ form separate bands. An increase of the excitation energy of the negative-parity band relative to that of the positive-parity ground-state band indicates a transition from octupole deformation to octupole vibrations [4].

In this section we analyze the theoretical spectroscopic properties that characterize the evolution of octupole deformation in the four isotopic chains. Part of the results for $^{220-230}$Th have been already reported in our recent study of Ref. [48], but are included here for completeness and compared to those obtained for Ra nuclei.

A. Systematics of excitation energies

In Fig. 11 we display the systematics of the calculated excitation energies of the positive-parity ground-state band ($K^\pi = 0^+$), and in Fig. 12 the lowest negative-parity ($K^\pi = 0^-$) sequences in $^{220-232}$Th, $^{218-228}$Ra, $^{146-156}$Sm, and $^{140-150}$Ba nuclei, in comparison with available data [64]. Firstly we note that, even without any additional adjustment of the parameters

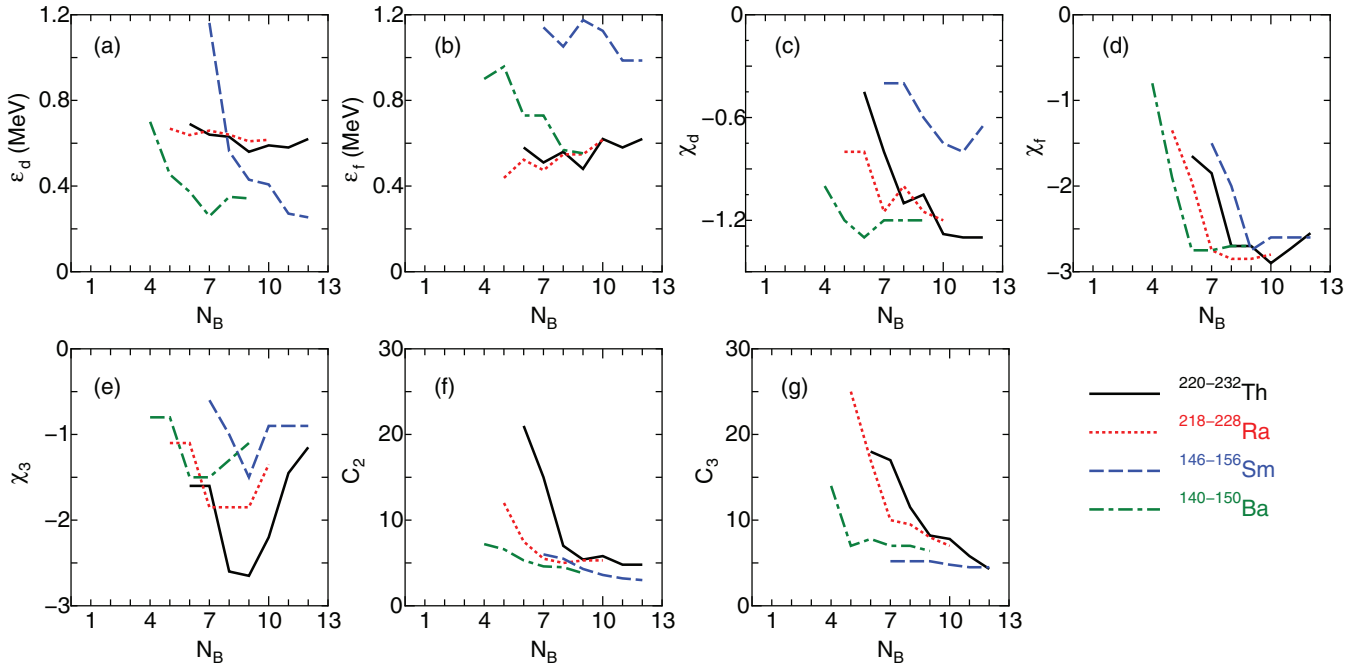

FIG. 10. (Color online) Total boson number N_B dependence of the parameters for the sdf IBM Hamiltonian Eq. (2): ϵ_d (a), ϵ_f (b), χ_d (b), χ_f (c), χ_f (d), and χ_3 (e), and the coefficient of the shape variables C_2 (f) and C_3 (g), determined by mapping the microscopic RHB energy surfaces onto the corresponding expectation values of the IBM Hamiltonian. Solid, dotted, dashed, and dot-dashed lines connect the parameters of the Th, Ra, Sm, and Ba isotopic chains, respectively.

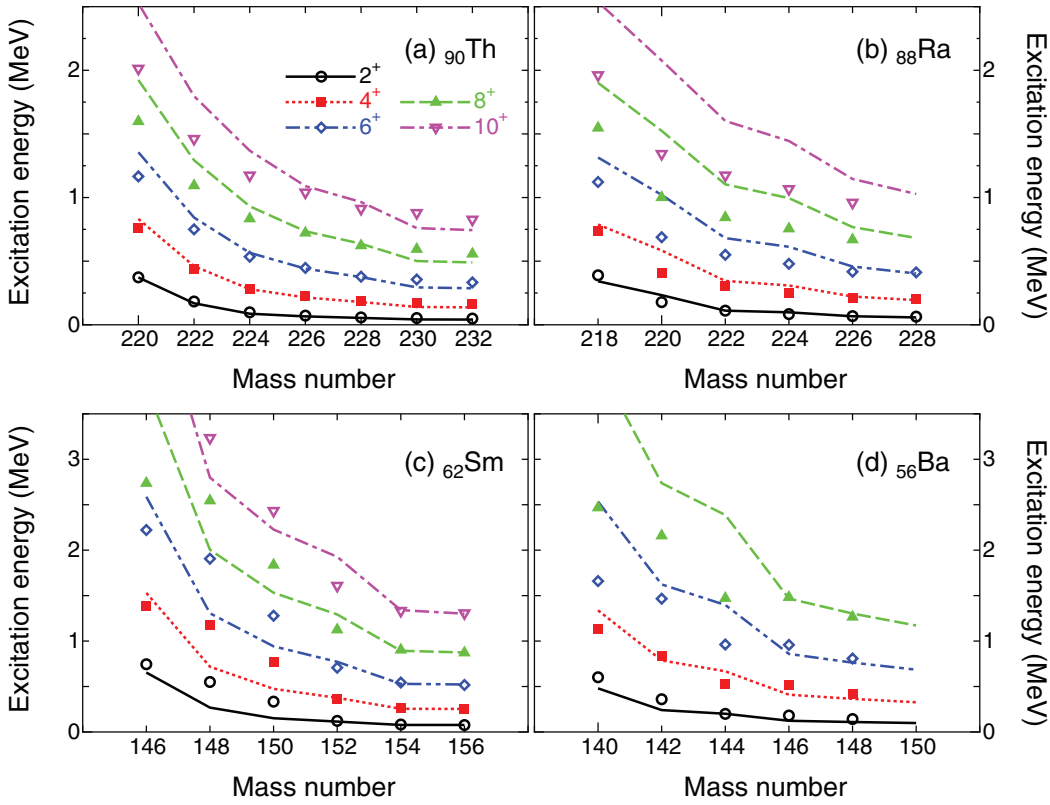

FIG. 11. (Color online) Excitation energies of low-lying yrast positive-parity collective states of $^{220-232}$Th, $^{218-228}$Ra, $^{146-156}$Sm, and $^{140-150}$Ba, as functions of the mass number. In each panel lines and symbols denote the theoretical and experimental [64] values, respectively. Figure legends are found in (a).

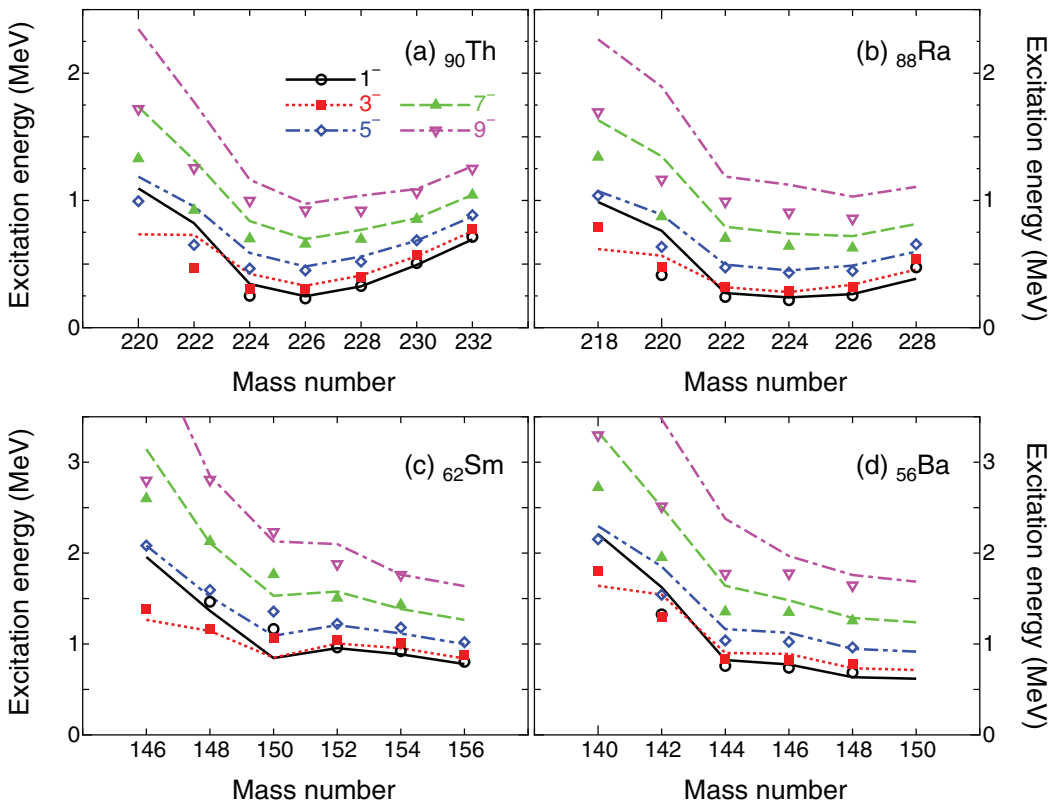

FIG. 12. (Color online) Same as in the caption to Fig. 11 but for the negative-parity states.

to data, that is, by using parameters determined exclusively by the microscopic calculation of potential energy surfaces, the IBM quantitatively reproduces the mass dependence of the excitation energies of levels that belong to the lowest bands of positive and negative parity.

The excitation energies of positive-parity states systematically decrease with mass number, reflecting the increase of quadrupole collectivity. For instance, ^{220,222}Th exhibit a quadrupole vibrational structure, whereas pronounced ground-state rotational bands with $R_{4/2} = E(4_1^+)/E(2_1^+) \approx 3.33$ are found in $^{226–232}$Th. For the nuclei ^{224,226}Th, located in the transitional region between quadrupole vibrators and axially deformed rotors, the experimental $R_{4/2}$ values are 2.90 and 3.14, respectively, the former being close to the value 2.91 predicted by the $X(5)$ model [65] for reflection-symmetric axially-deformed nuclei. In the calculation $R_{4/2} = 3.22$ and 3.26 for ^{224,226}Th, respectively. A similar systematics is found in the other isotopic chains [Figs. 11(b)–11(d)], that is, the evolution of quadrupole collectivity characterized by the lowering of the positive-parity ground-state band. However, the theoretical predictions for the positive-parity states overestimate the experimental values. The discrepancies are larger for the Ra and Ba isotopes because the boson model space is more restricted in comparison to the neighboring Th and Sm isotopes.

In the present analysis, however, we are more concerned with negative-parity states. For the states of the negative-parity band in Th isotopes the excitation energies display a parabolic structure centered between ^{224}Th and ^{226}Th [Fig. 12(a)]. The approximate parabola of 1_1^- states has a minimum at ^{226}Th, in which the octupole deformed minimum is most pronounced (cf. Figs. 1 and 9). Starting from ^{226}Th the energies of negative-parity states systematically increase and the band becomes more compressed. A rotational-like collective band based on the octupole vibrational state, i.e., the 1_1^- band head, develops.

For the Ra isotopes shown in Fig. 12(b) a similar trend, that is, an approximate parabola of negative-parity yrast states, is predicted particularly for states with spin $J^\pi = 1^-, 3^-$ and 5^-. One notices that the parabolic dependence is not as pronounced as in the Th case. The model predicts that the excitation energy of the 1_1^- state is lowest in ^{224}Ra. This result is consistent with the evolution of the experimental low-spin negative-parity states with neutron number [64], and also with the recent experimental study of stable octupole deformation in ^{224}Ra [6]. Namely, the experimental states 1_1^- (3_1^-) are observed at 242 (317) keV, 216 (290) keV, and 254 (322) keV, in ^{222,224,226}Ra, respectively [64]. On the other hand, in both the positive and negative parity bands some high-spin states, particularly for the lighter isotopes, are predicted at much higher energies compared to the data [64]. One of the reasons is certainly the restricted valence space from which boson states are built. The recent Hartree-Fock-Bogoliubov calculations [14,17], based on the Gogny D1S and D1M [66] functionals, reproduced the parabolic-like dependence of the 1_1^- state in the Ra isotopes as a function of N, similarly to the result obtained in the present study.

For the Sm [Fig. 12(c)] and Ba [Fig. 12(d)] isotopes, the mass dependence of negative-parity yrast states is more monotonic. For Sm the calculated excitation energies of both positive- and negative-parity states show a very weak variation with mass number starting from ^{152}Sm or ^{154}Sm. The octupole vibrational structure reflects the systematics of the deformation energy surfaces shown in Fig. 3. The yrast states of Ba isotopes display no significant structural change starting from ^{144}Ba or ^{146}Ba, that is, the excitation energies of both positive- and negative-parity yrast states look almost constant with mass (neutron) number. Note, however, that the calculated energy levels for Ba isotopes exhibit a more abrupt change from ^{144}Ba to ^{146}Ba, especially for higher-spin states. Other EDF-based approaches have predicted an isotopic dependence of the 1_1^- level of Ba isotopes (decrease in energy from ^{140}Ba to ^{144}Ba or ^{146}Ba) similar to the present result [14], but also a parabolic behavior for the Sm chain with a minimum at ^{150}Sm [16], rather different from the present trend shown in Fig. 12(c) and from the experimental excitation energies [64].

B. Transition between static octupole deformation and octupole vibrations

Another indication of a transition between octupole deformation and octupole vibrations for β_3-soft potentials is the odd-even staggering shown in Fig. 13. For both positive and negative parity, we plot the calculated ratios $E(J)/E(2_1^+)$ for the yrast states of $^{220–232}$Th, $^{218–228}$Ra, $^{146–156}$Sm, and $^{140–150}$Ba nuclei as functions of the angular momentum J, in comparison to data. For Th isotopes with $A \leqslant 226$ the odd-even staggering is negligible, indicating that positive- and negative-parity states belong to a single band, that is, the two bands are located close in energy. The staggering only becomes more pronounced starting from ^{228}Th, and this means that negative-parity states form a separate rotational-like collective band built on the octupole vibrational state. One notices that the predicted staggering of yrast states is in very good agreement with data [64]. For the Ra isotopes the staggering becomes visible starting with ^{226}Ra, but is much less pronounced compared to the Th nuclei with the same number of neutrons.

Similarly, the odd-even staggering is more pronounced in Sm than in Ba. For the Sm isotopes the effect becomes significant starting from ^{152}Sm, but is negligible for $A \leqslant 150$. Note that ^{150}Sm exhibits the deepest octupole minimum in the deformation energy surface (Fig. 3). The staggering pattern in Sm isotopes, shown in Figs. 13(e) and 13(f), appears slightly different from the one obtained for the Th isotopes [Figs. 13(a) and 13(b)]. For the latter case the amplitude of the staggering keeps increasing with mass number, whereas it shows very little variation in the Sm chain starting from ^{152}Sm. This feature reflects the fact that the β_3-softness of the potential does not show significant variations between ^{152}Sm and ^{156}Sm. A similar trend, but with much less prominent staggering, is observed for the Ba nuclei in Figs. 13(g) and 13(h).

The emergence of octupole vibrational states can be further analyzed by computing the energy displacement $\delta E(J)$ between positive- and negative-parity bands, defined as [9]

$$\delta E(J) = E(J^-) - \frac{\{E((J+1)^+) + E((J-1)^+)\}}{2}. \quad (14)$$

For a stable octupole deformed nucleus, in which the positive- and negative-parity yrast states form an alternating-parity

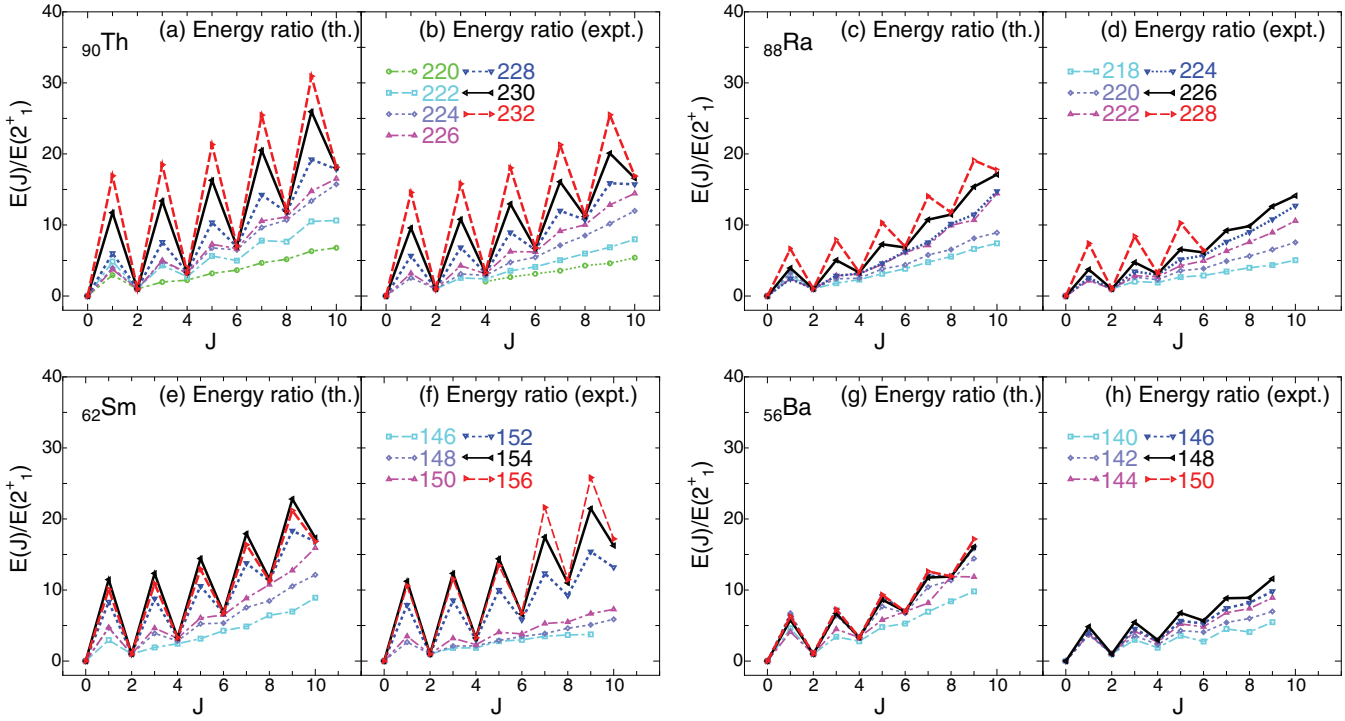

FIG. 13. (Color online) Theoretical and experimental [64] energy ratios $E(J^\pi)/E(2_1^+)$ for states of the positive-parity ground-state band (J even) and the lowest negative-parity band (J odd), as functions of the angular momentum J, for $^{220-232}$Th (a), (b), $^{218-228}$Ra (c), (d), $^{146-156}$Sm (e), (f), and $^{140-150}$Ba (g), (h).

band, $\delta E(J)$ should be approximately zero. The deviation from the limit $\delta E = 0$ indicates the decoupling of states with positive and negative parity, thus pointing to the occurrence of octupole vibrational states.

Figure 14 displays the calculated $\delta E(J)$ values for the four isotopic chains, normalized with respect to the excitation energy of 2_1^+, as functions of the mass number. The theoretical values are compared to data from Ref. [64]. As one would expect, the $\delta E(J)/E(2_1^+)$ values begin to show a significant increase starting from a specific isotope in the Th, Ra, and Sm chains, that is, from ^{226}Th, ^{224}Ra, and ^{150}Sm, for which a stable octupole deformation appears on the corresponding DD-PC1 energy surface (cf. Figs. 1–3), and is also reflected in the plot of excitation energies [cf. Figs. 11(a)–11(c) and 12(a)–12(c)]. For the Ba isotopes, on the other hand, no significant increase is observed in the variation of the $\delta E(J)/E(2_1^+)$ value with mass number.

C. Systematics of $E1$ and $E3$ transitions

In addition to the comparison between the calculated and the experimental energy spectra, in this section we examine the $E3$ and $E1$ properties, which also provide signatures for the onset of octupole deformation. In Fig. 15 we display the isotopic dependence of the $B(E3; 3_1^- \rightarrow 0_1^+)$ [panels (a) to (d)] and $B(E1; 1_1^- \rightarrow 0_1^+)$ [panels (e) to (h)] values for $^{220-232}$Th, $^{218-228}$Ra, $^{146-156}$Sm, and $^{140-150}$Ba, in comparison to available data [4–6,64,67–69].

The $E3$ transition strength, in particular, can be regarded as a good measure of octupole collectivity [4]. The upper part of Fig. 15 [panels (a) to (d)] shows that the present calculation yields $B(E3; 3_1^- \rightarrow 0_1^+)$ values that are consistent with the experimental trend. In the Th, Ra, and Sm isotopic chains

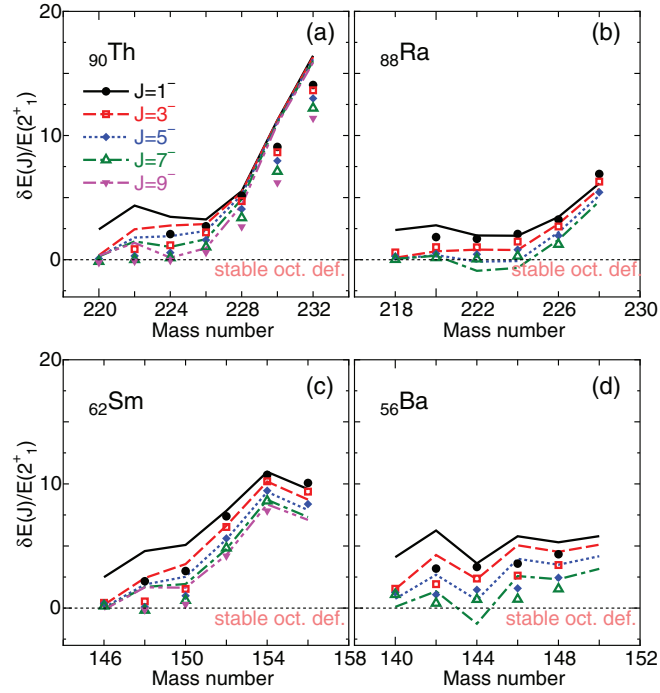

FIG. 14. (Color online) The energy displacement $\delta E(J)$ [defined in Eq. (14)] normalized with respect to the excitation energy of 2_1^+, as a function of the mass number. The limit of stable octupole deformation $\delta E(J) = 0$ is indicated by the dotted horizontal line. Experimental data, represented symbols in each panel, are taken from Ref. [64].

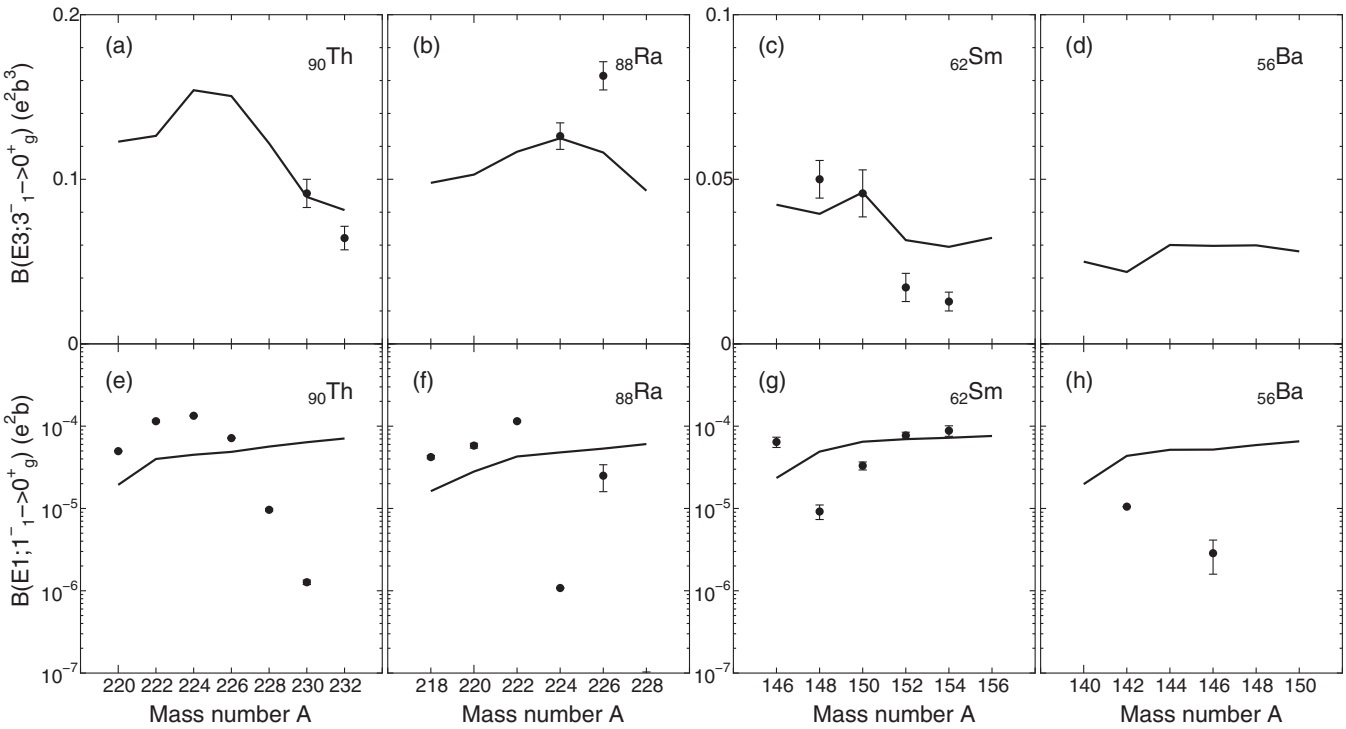

FIG. 15. Isotopic dependence of the $B(E3; 3_1^- \rightarrow 0_1^+)$ [(a) to (d)] and $B(E1; 1_1^- \rightarrow 0_1^+)$ [(e) to (h)] values for $^{220-232}$Th, $^{218-228}$Ra, $^{146-156}$Sm, and $^{140-150}$Ba. The vertical axes for (e)–(h) are in logarithmic scale. Solid lines connect calculated values, symbols denote data taken from Refs. [4–6,64,67–69].

the theoretical $B(E3; 3_1^- \rightarrow 0_1^+)$ values reach a maximum for ^{226}Th, ^{224}Ra, and ^{150}Sm, respectively, that is, for isotopes in which the octupole deformation minimum is most prominent (Figs. 1–3). In the Ba chain the theoretical $B(E3)$ values remain almost constant with increasing neutron number, reflecting the fact that no shape transition is predicted by the calculation.

For all the considered isotopic chains, in contrast to the systematics of the energy surfaces, the excitation spectra, and the $B(E3; 3_1^- \rightarrow 0_1^+)$ values, the calculated $B(E1; 1_1^- \rightarrow 0_1^+)$ values exhibit only a monotonic increase as functions of the mass number. The corresponding experimental values seem to suggest more significant structural changes in the isotopic sequences. In fact, only for the $^{148-154}$Sm nuclei the present calculation qualitatively reproduces the experimental trend in heavier isotopes [Fig. 15(g)]. On the other hand, much larger $B(E1; 1_1^- \rightarrow 0_1^+)$ values, by $\approx 10^{2-4}$ compared to experimental ones, are predicted for the heavier Th and Ra isotopes, as well as for the Ba nuclei.

There are several possible reasons for the systematic discrepancy between theoretical and empirical $B(E1)$ values. Firstly, the choice of the fixed effective charge $e_1 = 0.01eb^{1/2}$ [60] might be too restricted and, in principle, one could allow a variation of the effective charge with mass number. For the Ra isotopes [Fig. 15(f)], for instance, a sudden decrease of the experimental $B(E1; 1_1^- \rightarrow 0_1^+)$ value from ^{222}Ra to ^{224}Ra could reflect a complex change of structure. Such an effect could easily be absorbed in the variation of the effective charge. Moreover, the present model considers only isoscalar properties, that is, there is no distinction between proton and neutron bosons, whereas for $E1$ transitions isovector components could play an important role. Secondly, the form of the $E1$ operator $\hat{T}^{(E1)}$ in Eq. (10) may need to be extended. In fact, it has been shown that in the sdf IBM two-body terms should be included in the $E1$ operator [70]. Such an extension invokes additional parameters for the $E1$ operator, but these would be difficult to determine uniquely. Most likely, however, the model space of s, d, and f bosons is by construction not sufficient to describe the $E1$ systematics. This implies that the inclusion of the p ($J^\pi = 1^-$) boson might be necessary. Actually, as shown by Otsuka [54], intrinsic wave functions of quadrupole-octupole deformed nuclei could contain a large fraction of the dipole nucleon pair. An extension of our model along these lines could be an interesting subject for a future study.

In some previous phenomenological sdf (or $spdf$) IBM studies, the $B(E1; 1_1^- \rightarrow 0_1^+)$ values for Sm isotopes were reproduced slightly better than in the present calculation (see, e.g., [18]). In Ref. [18], however, two-body terms have been added to the $E1$ operator. The recent two-dimensional (2D) GCM calculation for Sm isotopes [16], based on the Gogny effective interaction, has reproduced the experimental $B(E1; 1_1^- \rightarrow 0_1^+)$ values with a more or less similar level of agreement as the present work. Other beyond-mean-field studies of Ra and Ba isotopes [14], and Ra-Th isotopes [17], that used the collective Hamiltonian approach based on the Gogny D1S and the BCP functional, and the 2D GCM approach with the Gogny D1S and D1M interactions, respectively, have reported results for $B(E1; 1_1^- \rightarrow 0_1^+)$ that are more consistent with the experimental systematics.

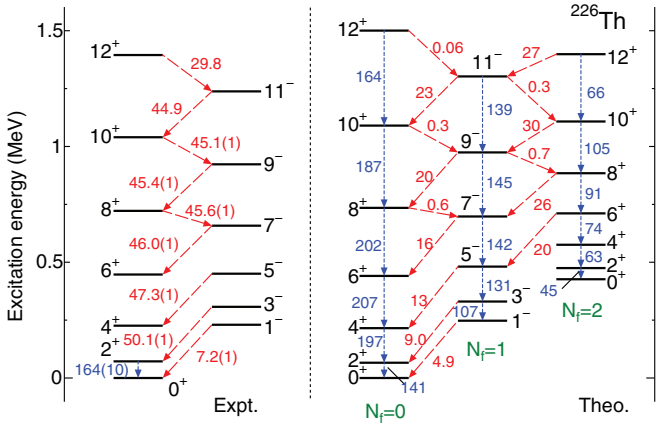

FIG. 16. (Color online) Partial level scheme of ^{226}Th. The theoretical low-lying spectra, in-band $B(E2)$ values (in Weisskopf units, dotted arrows), and interband $B(E1)$ values (in units of $e^2\mathrm{b}\times10^{-5}$, dashed arrows), are compared to available data [4,5,64].

D. Detailed level schemes

To illustrate in more detail the level of quantitative agreement between our microscopic model calculation and data, we analyze the low-lying energy spectra of positive- and negative-parity states, the $B(E2)$ values for in-band transitions, and the interband $B(E1)$ values, for the octupole-deformed nucleus ^{226}Th (Fig. 16), and the octupole-soft nucleus ^{230}Th (Fig. 17).

The level scheme of ^{226}Th (Fig. 16) shows that the lowest negative-parity band (composed of one-f-boson states) is located close in energy to the ground-state positive-parity band (comprised of positive-parity bosons only, that is, $N_f = 0$). One notices that the lowest positive- and negative-parity bands form a single, alternating-parity band, starting with angular momentum $J = 5$. Overall, a very good agreement between theory and experiment is obtained for the excitation spectrum of ^{226}Th. Strong $E1$ transitions are predicted from odd-J states of the negative-parity band to the even $(J-1)$ states of the ground-state positive-parity band, in agreement with data. However, the calculated $E1$ transitions in the inverse direction [from even-J to the odd $(J-1)$ states] are considerably weaker, whereas the experimental values are of the same order as for the former transitions. The opposite systematics is predicted for the $E1$ transitions between the negative-parity band $N_f = 1$ and the second-lowest positive-parity band $N_f = 2$ (built on two-f-boson states), that is, the $E1$ transitions from even-J states to the odd $(J-1)$ states dominate.

For the nucleus ^{230}Th we notice in Fig. 17 that the present calculation reproduces very well the experimental [64] energy levels of the positive-parity ground-state ($K^\pi = 0^+$) band, including the $E2$ transition strengths, and those of the two lowest ($K^\pi = 0^-$ and 1^-) negative parity bands. Compared to ^{226}Th, the band $K^\pi = 0^-$ is found at much higher excitation energy, consistent with the picture of octupole vibrations. However, the theoretical positive-parity bands built on the 0_2^+ state and the 2_3^+ state, are predicted high above their experimental counterparts. The reason could be the too large value for the quadrupole-quadrupole interaction strength κ_2, which is relevant for the band-head energies of the side bands. In fact, the present κ_2 value is more than three times larger than the one used in the previous IBM phenomenological study [22]. This value reflects the pronounced quadrupole deformation minimum predicted by the RHB energy surface. $E2$ transitions between the states of the positive-parity ground-state band and the two side bands built on 0_2^+ and 2_3^+ vanish, and this means there is no mixing between the corresponding configurations. In fact, for ^{230}Th the IBM model predicts that the states in the ground-state are composed of s and d bosons only, that is, $N_f = 0$, whereas those of the two positive-parity side bands are built on two-f-boson states (Fig. 17). The low-lying negative-parity states are, of course, of one-f-boson nature.

E. The nucleus ^{224}Ra

Finally, we compare the results of the present microscopic calculation with very recent data for the octupole deformed nucleus ^{224}Ra, obtained in the Coulomb excitation experiment

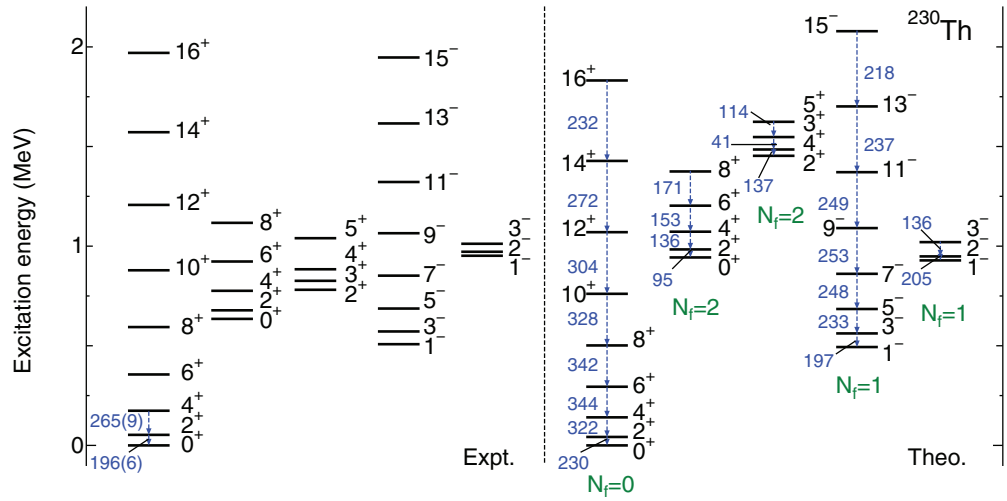

FIG. 17. (Color online) Partial level scheme of ^{230}Th. The theoretical low-lying spectra and in-band $B(E2)$ values (in Weisskopf units, dotted arrows) are compared to available data [64].

TABLE I. Comparison between experimental [6] and theoretical $B(E\lambda)$ values for transitions in ^{224}Ra (in Weisskopf units). All transitions shown in the table, except for the $E2$ transition from the band head of the band built on the 2_2^+ state to the 0^+ ground state, are between yrast states.

	Expt. (W.u.)	Theor. (W.u.)
$B(E2;2^+ \to 0^+)$	98 ± 3	109
$B(E2;3^- \to 1^-)$	93 ± 9	71
$B(E2;4^+ \to 2^+)$	137 ± 5	152
$B(E2;5^- \to 3^-)$	190 ± 60	97
$B(E2;6^+ \to 4^+)$	156 ± 12	159
$B(E2;8^+ \to 6^+)$	180 ± 60	153
$B(E2;2_2^+ \to 0^+)$	1.3 ± 0.5	0
$B(E3;3^- \to 0^+)$	42 ± 3	42
$B(E3;1^- \to 2^+)$	210 ± 40	85
$B(E3;3^- \to 2^+)$	<600	46
$B(E3;5^- \to 2^+)$	61 ± 17	61
$B(E1;1^- \to 0^+)$	$<5 \times 10^{-5}$	2.0×10^{-3}
$B(E1;1^- \to 2^+)$	$<1.3 \times 10^{-4}$	1.1×10^{-3}
$B(E1;3^- \to 2^+)$	$3.9^{+1.7}_{-1.4} \times 10^{-5}$	3.7×10^{-3}
$B(E1;5^- \to 4^+)$	$4^{+3}_{-2} \times 10^{-5}$	5.0×10^{-3}
$B(E1;7^- \to 6^+)$	$<3 \times 10^{-4}$	5.8×10^{-3}

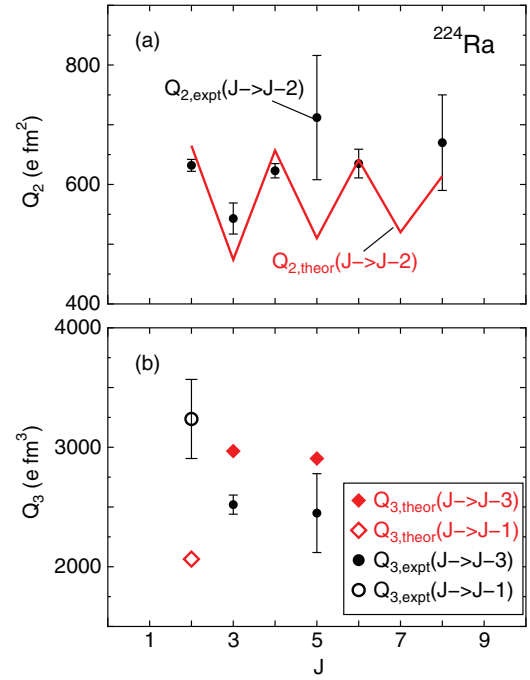

FIG. 18. (Color online) Comparison between the experimental [6] and calculated quadrupole and octupole intrinsic moments of ^{224}Ra, as functions of the angular momentum J^π ($\pi = +1$ and -1 for J even and odd, respectively).

of Ref. [6]. Table I lists all the experimental $B(E\lambda)$ values included in Ref. [6], in comparison with our model results. For the $E2$ transition rates a very good agreement is obtained between the experimental and the calculated values, possibly with the exception of the $5^- \to 3^-$ transition which is underestimated in the calculation. We also note the nice agreement of the $B(E3; J \to J-3)$ values, but the calculated $B(E3; 1^- \to 2^+)$ is considerably smaller than the experimental value. On the other hand, the theoretical $B(E1)$ values are systematically too large, typically by 10^1–10^2, when compared with data. Possible reasons for this discrepancy have been addressed in Sec. IV C.

In Fig. 18 we plot the $E2$ and $E3$ intrinsic moments determined from the $B(E2)$ and the $B(E3)$ values listed in Table I, using the relation given in Eq. (13). One notes a staggering in the calculated $Q_2(J \to J-2)$ values, and their average value $\approx$600 $e$fm^2 is consistent with the measured value [6]. The same observation applies to the octupole intrinsic moment Q_3. The mean value of the three Q_3 moments is approximately 2500 $e$fm^3, in agreement with experiment.

V. SUMMARY AND CONCLUDING REMARKS

In the present study we have performed a microscopic analysis of octupole shape transitions in four isotopic chains characteristic for two regions of octupole deformation and collectivity: Th, Ra, Sm, and Ba. As a microscopic input we have used the axial quadrupole-octupole deformation energy surfaces calculated employing the relativistic Hartree-Bogoliubov model based on the universal energy density functional DD-PC1 which has, of course, not been specifically adjusted to octupole deformed nuclei. By mapping the deformation-constrained microscopic energy surfaces onto the equivalent sdf IBM Hamiltonian, that is, onto the corresponding expectation values of the IBM Hamiltonian in boson coherent states, the Hamiltonian parameters have been determined without any specific adjustment to experimental spectra. The mapped sdf IBM Hamiltonian has been used to calculate low-energy spectra and transition rates for both positive- and negative-parity states of the four sequences of isotopes. The systematics of the axially-symmetric (β_2,β_3) energy surface (from Figs. 1 to 8), the average value of the octupole deformation $\langle\beta_3\rangle$ (Fig. 9), the variation of the resulting Hamiltonian parameters (Fig. 10), the calculated excitation spectra (Figs. 11–14), and the $E3$ transition rates (Fig. 15), show a consistent picture of evolution of octupole correlations in the two regions of medium-heavy and heavy nuclei.

The microscopic DD-PC1 energy surfaces suggest a transition from nonoctupole (quadrupole vibrational) to stable octupole deformed, and to octupole vibrations characteristic for β_3-soft potentials, in the Th, Ra, and Sm isotopic chains. Among all nuclei considered in this work, the Th isotopes appear to present the best case for the evolution of octupole correlations. The calculated excitation spectra of all considered isotopes exhibit a decrease in energy of states in the positive-parity ground-state band with the increase of the neutron number (Fig. 11), in agreement with available data. The evolution of the ground-state bands with neutron number clearly shows the transition from spherical vibrators to quadrupole deformed rotors. For the Th and the Ra isotopes (Fig. 12) the states in the lowest negative-parity band display a parabolic energy dependence on the mass number, with energy minima at ^{226}Th and ^{224}Ra that correspond to stable octupole deformations, consistent with the evolution of the microscopic

energy surfaces (Figs. 1 and 2). The approximate parabolas of low-spin negative-parity states can be identified as signatures of the transition from stable octupole deformation to octupole vibrations. In the case of Sm and Ba isotopes, the evolution of the lowest negative-parity band is much more moderate, and the excitation energies of negative-parity states show almost no variation for heavier isotopes. This means that the β_3-soft octupole potentials do not change with neutron number, and the spectra are those of octupole vibrators.

For most nuclei considered in the present analysis the IBM model based on microscopic deformation energy surfaces produces results in a reasonable agreement with available experimental spectroscopic properties. Nevertheless, considerable disagreement has been found for higher-spin states, particularly for those nuclei for which the space of boson states appear to be too restricted. In particular, the present model calculation has apparently failed in the description of the $E1$ transition rates [Figs. 15(e)–15(h) and 16]. We have discussed several possible reasons: (i) the oversimplified parametrization of the $E1$ effective charge, (ii) the restricted form of the adopted $E1$ operator, and (iii) the insufficient sdf model space that could be extended by the inclusion of other types of bosons. A complete analysis of $E1$ systematics will be the topic of a future study.

ACKNOWLEDGMENTS

The authors would like to thank R. V. Jolos and J. Zhao for useful discussions. K. N. acknowledges the support by the Marie Curie Actions grant within the Seventh Framework Program of the European Commission under Grant No. PIEF-GA-2012-327398. Calculations were partly performed on the ScGrid of the Supercomputing Center, Computer Network Information Center of Chinese Academy of Sciences.

[1] A. Bohr and B. M. Mottelsson, *Nuclear Structure*, Vol. 2 (Benjamin, New York, USA, 1975).
[2] P. Ring and P. Schuck, *The Nuclear Many-Body Problem* (Springer-Verlag, Berlin, 1980).
[3] R. F. Casten, *Nuclear Structure from a Simple Perspective* (Oxford University Press, Oxford, 2000).
[4] P. A. Butler and W. Nazarewicz, Rev. Mod. Phys. **68**, 349 (1996).
[5] P. A. Butler and W. Nazarewicz, Nucl. Phys. A **533**, 249 (1991).
[6] L. P. Gaffney, P. A. Butler, M. Scheck, A. B. Hayes, F. Wenander, M. Albers, B. Bastin, C. Bauer, A. Blazhev, S. Bönig *et al.*, Nature (London) **497**, 199 (2013).
[7] P. E. Garrett, W. D. Kulp, J. L. Wood, D. Bandyopadhyay, S. Choudry, D. Dashdorj, S. R. Lesher, M. T. McEllistrem, M. Mynk, J. N. Orce *et al.*, Phys. Rev. Lett. **103**, 062501 (2009).
[8] S. Marcos, H. Flocard, and P. H. Heenen, Nucl. Phys. A **410**, 125 (1983).
[9] W. Nazarewicz, P. Olanders, I. Ragnarsson, J. Dudek, G. A. Leander, P. Möller, and E. Ruchowsa, Nucl. Phys. A **429**, 269 (1984).
[10] W. Nazarewicz and P. Olanders, Nucl. Phys. A **441**, 420 (1985).
[11] P. Bonche, P.-H. Heenen, H. Flocard, and D. Vautherin, Phys. Lett. B **175**, 387 (1986).
[12] P. Bonche, in *The Variation of Nuclear Shapes*, edited by J. D. Garrett (World Scientific, Singapore, 1988), p. 302.
[13] J. L. Egido and L. M. Robledo, Nucl. Phys. A **524**, 65 (1991).
[14] L. M. Robledo, M. Baldo, P. Schuck, and X. Viñas, Phys. Rev. C **81**, 034315 (2010).
[15] L. M. Robledo and G. F. Bertsch, Phys. Rev. C **84**, 054302 (2011).
[16] R. Rodríguez-Guzmán, L. M. Robledo, and P. Sarriguren, Phys. Rev. C **86**, 034336 (2012).
[17] L. M. Robledo and P. A. Butler, Phys. Rev. C **88**, 051302(R) (2013).
[18] O. Scholten, F. Iachello, and A. Arima, Ann. Phys. (NY) **115**, 325 (1978).
[19] J. Engel and F. Iachello, Nucl. Phys. A **472**, 61 (1987).
[20] T. Otsuka and M. Sugita, Phys. Lett. B **209**, 140 (1988).
[21] D. Kusnezov and F. Iachello, Phys. Lett. B **209**, 420 (1988).
[22] P. D. Cottle and N. V. Zamfir, Phys. Rev. C **58**, 1500 (1998).
[23] P. G. Bizzeti and A. M. Bizzeti-Sona, Phys. Rev. C **70**, 064319 (2004).
[24] D. Bonatsos, D. Lenis, N. Minkov, D. Petrellis, and P. Yotov, Phys. Rev. C **71**, 064309 (2005).
[25] D. Lenis and D. Bonatsos, Phys. Lett. B **633**, 474 (2006).
[26] P. G. Bizzeti and A. M. Bizzeti-Sona, Phys. Rev. C **77**, 024320 (2008).
[27] P. G. Bizzeti and A. M. Bizzeti-Sona, Phys. Rev. C **81**, 034320 (2010).
[28] R. V. Jolos, P. von Brentano, and J. Jolie, Phys. Rev. C **86**, 024319 (2012).
[29] N. Minkov, S. Drenska, M. Strecker, W. Scheid, and H. Lenske, Phys. Rev. C **85**, 034306 (2012).
[30] P. G. Bizzeti and A. M. Bizzeti-Sona, Phys. Rev. C **88**, 011305(R) (2013).
[31] F. Iachello and A. D. Jackson, Phys. Lett. B **108**, 151 (1982).
[32] H. J. Daley and F. Iachello, Ann. Phys. (NY) **167**, 73 (1986).
[33] T. M. Shneidman, G. G. Adamian, N. V. Antonenko, R. V. Jolos, and W. Scheid, Phys. Lett. B **526**, 322 (2002).
[34] W. Zhang, Z. P. Li, S. Q. Zhang, and J. Meng, Phys. Rev. C **81**, 034302 (2010).
[35] B.-N. Lu, E.-G. Zhao, and S.-G. Zhou, Phys. Rev. C **85**, 011301(R) (2012).
[36] B.-N. Lu, J. Zhao, E.-G. Zhao, and S.-G. Zhou, Phys. Rev. C **89**, 014323 (2014).
[37] M. Bender, P.-H. Heenen, and P.-G. Reinhard, Rev. Mod. Phys. **75**, 121 (2003).
[38] T. H. R. Skyrme, Nucl. Phys. **9**, 615 (1958).
[39] D. Vautherin and D. M. Brink, Phys. Rev. C **5**, 626 (1972).
[40] J. Decharge, M. Girod, and D. Gogny, Phys. Lett. B **55**, 361 (1975).
[41] D. Vretenar, A. V. Afanasjev, G. Lalazissis, and P. Ring, Phys. Rep. **409**, 101 (2005).
[42] T. Nikšić, D. Vretenar, and P. Ring, Prog. Part. Nucl. Phys. **66**, 519 (2011).
[43] K. Nomura, N. Shimizu, and T. Otsuka, Phys. Rev. Lett. **101**, 142501 (2008).
[44] F. Iachello and A. Arima, *The Interacting Boson Model* (Cambridge University Press, Cambridge, 1987).

[45] K. Nomura, T. Otsuka, N. Shimizu, and L. Guo, Phys. Rev. C **83**, 041302(R) (2011).
[46] K. Nomura, N. Shimizu, D. Vretenar, T. Nikšić, and T. Otsuka, Phys. Rev. Lett. **108**, 132501 (2012).
[47] K. Nomura, R. Rodríguez-Guzmán, L. M. Robledo, and N. Shimizu, Phys. Rev. C **86**, 034322 (2012).
[48] K. Nomura, D. Vretenar, and B.-N. Lu, Phys. Rev. C **88**, 021303(R) (2013).
[49] A. Arima and F. Iachello, Ann. Phys. (NY) **111**, 201 (1978).
[50] T. Nikšić, D. Vretenar, and P. Ring, Phys. Rev. C **78**, 034318 (2008).
[51] Y. Tian, Z. Y. Ma, and P. Ring, Phys. Lett. B **676**, 44 (2009).
[52] T. Otsuka, A. Arima, and F. Iachello, Nucl. Phys. A **309**, 1 (1978).
[53] A. F. Barfield, B. R. Barrett, J. L. Wood, and O. Scholten, Ann. Phys. (NY) **182**, 344 (1988).
[54] T. Otsuka, Phys. Lett. B **182**, 256 (1986).
[55] N. V. Zamfir and D. Kusnezov, Phys. Rev. C **63**, 054306 (2001).
[56] M. Sugita, T. Otsuka, and P. von Brentano, Phys. Lett. B **389**, 642 (1996).
[57] K. Nomura, N. Shimizu, and T. Otsuka, Phys. Rev. C **81**, 044307 (2010).
[58] J. N. Ginocchio and M. W. Kirson, Nucl. Phys. A **350**, 31 (1980).
[59] D. Kusnezov, computer program OCTUPOLE (unpublished).
[60] M. Babilon, N. V. Zamfir, D. Kusnezov, E. A. McCutchan, and A. Zilges, Phys. Rev. C **72**, 064302 (2005).
[61] J. F. Berger, M. Girod, and D. Gogny, Nucl. Phys. A **428**, 23 (1984).
[62] M. Baldo, P. Schuck, and X. Viñas, Phys. Lett. B **663**, 390 (2008).
[63] W. Long, J. Meng, N. Van Giai, and S.-G. Zhou, Phys. Rev. C **69**, 034319 (2004).
[64] Brookhaven National Nuclear Data Center, http://www.nndc.bnl.gov.
[65] F. Iachello, Phys. Rev. Lett. **87**, 052502 (2001).
[66] S. Goriely, S. Hilaire, M. Girod, and S. Péru, Phys. Rev. Lett. **102**, 242501 (2009).
[67] F. R. Metzger, Phys. Rev. C **14**, 543 (1976).
[68] T. Kibédi and R. H. Spear, At. Data Nucl. Data Tables **80**, 35 (2002).
[69] H. Wollersheim, H. Emling, H. Grein, R. Kulessa, R. Simon, C. Fleischmann, J. de Boer, E. Hauber, C. Lauterbach, C. Schandera *et al*., Nucl. Phys. A **556**, 261 (1993).
[70] A. F. Barfield, P. von Brentano, A. Dewald, K. O. Zell, N. V. Zamfir, D. Bucurescu, M. Ivascu, and O. Scholten, Z. Phys. A **332**, 29 (1989).